Available online at www.sciencedirect.com
ScienceDirect
European Journal of Mechanics B/Fluids 26 (2007) 479–493

Analysis of the flow in a thermo-acoustic MHD generator with conducting walls

Cédric Vogin, Antoine Alemany *

Laboratory EPM, ENSHMG-BP 95, 38402, St-Martin d'Hères cedex, France

Received 16 January 2006; received in revised form 5 September 2006; accepted 26 October 2006

Available online 20 February 2007

Abstract

This paper is devoted to the analysis of a pulsating MHD flow in a rectangular channel, submitted to an applied DC magnetic field and an imposed harmonically oscillating thermo-acoustically generated pressure gradient. The resulting AC current is collected by two electrodes placed on one either side of the channel. The walls of the channel are assumed electrically conducting. The channel is considered sufficiently long to justify the hypothesis of a fully developed flow. The analytical solution proposed is based on a simultaneous resolution of the Navier–Stokes and induction equations. This solution is limited to moderate values of the magnetic Reynolds number.

Keywords: Magneto-hydrodynamics; Thermo-acoustic; Electric generator

1. Introduction

The thermo-acoustic generator [1] transforms heat into mechanical energy. The principle of the thermo-acoustic effect is based on the application of a temperature gradient imposed across a stack of plates. When the temperature gradient reaches a sufficiently high value, a pressure wave forms, which propagates along the closed thermo-acoustic tube at the velocity of sound.

An MHD generator channel is connected in series with the thermo-acoustic tube. The pressure oscillations produce velocity oscillations that can be converted into electricity by interaction with an externally applied magnetic field. The system is schematised in Fig. 1. This thermodynamic process thus allows direct conversion of heat into electricity without any moving mechanical part and without any fluid loop. It is very simple and has numerous possible industrial applications. It is compatible with any heat source and can be adapted for use on isolated sites (in space for example), at moderate power levels. The process is much simpler than the previous MHD power generator, which was based on the use of a double liquid/gas loop [2–4].

The present work is focused on the characterisation of the MHD channel, where the transformation of mechanical energy into electrical energy occurs. In particular, it is concerned with the oscillating flow in a very long MHD channel of rectangular cross-section and thin conductive walls (Fig. 2). The length L_B of the channel is much greater than the

* Corresponding author.
E-mail address: antoine.alemany@hmg.inpg.fr (A. Alemany).

0997-7546/$ – see front matter
doi:10.1016/j.euromechflu.2006.10.006

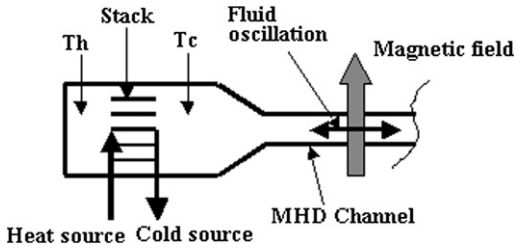

Fig. 1. Schematic representation of the thermo-acoustic engine coupled with an MHD generator.

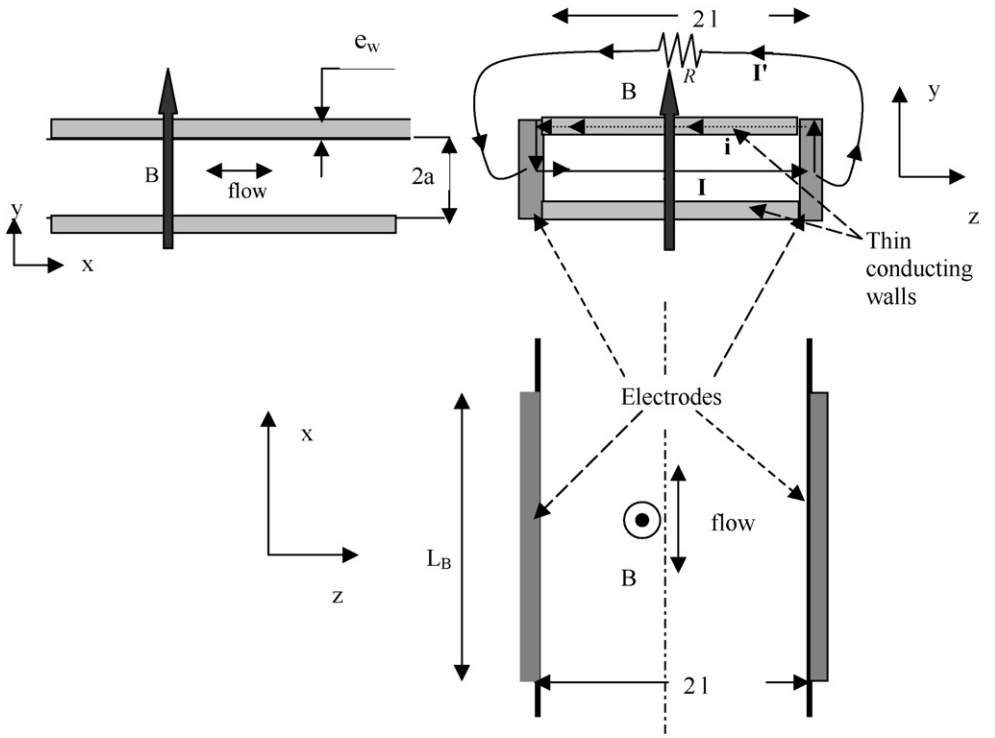

Fig. 2. Views of the MHD channel. The vertical magnetic field interacts with the pulsating flow. The resulting current is collected by two lateral electrodes.

other dimensions (width $2l$ and thickness $2a$) so it can be considered as infinitely long. The wall thickness of this channel e_w and its electrical conductivity σ_w are such that the thin wall hypothesis can be assumed [5,6]. A liquid metal of density ρ, dynamic viscosity μ, magnetic permeability μ_0 and electrical conductivity σ, oscillates in the channel in the x direction with a velocity amplitude u_0 and a pulsation ω. This occurs due to the oscillatory pressure gradient of amplitude $\Delta p/L_B$. The oscillating flow in the MHD channel is submitted to a constant external magnetic field $\vec{B}_0 = B_0\vec{e}_y$ imposed by an inductor. This generates an AC electrical current following from the interaction between the magnetic and the velocity fields. The current is collected by two electrodes placed at $z = \pm l$ (Fig. 2) which are used to supply a load which is here assimilated by the resistance R (Figs. 2, 3).

The influence of conducting walls on a low magnetic Reynolds number steady state MHD flow has been studied by relatively few authors (see for example Cuevas [7]) while the pulsating MHD flow has only been studied for the case of insulating walls (see Ibanez et al. [8]). The present study of the pulsating MHD flow assumes that the walls of the channel are electrically conducting and takes into account the influence of the magnetic Reynolds number R_m (this will be defined later in the text).

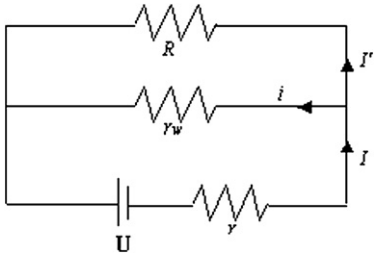

Fig. 3. Equivalent electrical circuit of the generator. The electric lines close partially in the load and partially in the channel walls. The part of the electric current closing in the boundary layers is not represented here.

The study combines the competition of two phenomena, which govern the flow configuration: the inertial effect and the magnetic field effect. In this work an exact analytical solution for both the velocity and induced magnetic field in a non-stationary (i.e. pulsating) flow is given.

The method of resolution is based on the characterisation of the magnetic field perturbation to determine the electromagnetic force field. In other studies the hypothesis of low magnetic Reynolds number is used to justify neglecting the induced field in the formulation of the problem (see for example the Ibanez et al. [8]).

The influence of the wall conductivity is taken into account, whereas other studies apply conditions of either insulating walls or perfectly conducting walls, which can lead to over-simplification of the boundary conditions. The concept of the wall conductance ratio [5,6] used in the formulation of the problem means that the wall conductivity can now be included in the boundary conditions. This of course supposes a homogeneous distribution of the electric current in the wall (small wall hypothesis). This hypothesis can be used in the following condition:

The depth of penetration, δ_p, of the oscillating magnetic perturbations with a pulsation frequency ω, inside the wall, is to a good approximation:

$$\delta_p \approx \sqrt{\frac{1}{\mu_0 \sigma_w \omega}},$$

the wall magnetic permeability, μ_0, is taken equal to that of the fluid. Assuming that the induced magnetic field, and consequently the induced electric current, is uniformly distributed in the wall (e_w) so that $\delta_p > e_w$, then one can write:

$$\frac{\delta_p}{e_w} = \sqrt{\frac{1}{\mu_0 \sigma_w \omega e_w^2}} > 1 \rightarrow \mu_0 \sigma_w \omega e_w^2 < 1.$$

By introducing the electrical conductivity of the fluid, σ, and the thickness a of the MHD channel (see Fig. 2), the above expression can be written as:

$$\mu_0 \sigma \omega a^2 \left(\frac{e_w^2 \sigma_w}{a^2 \sigma} \right) < 1 \rightarrow R_m \left(\frac{e_w^2 \sigma_w}{a^2 \sigma} \right) < 1.$$

This expression contains the non-dimensional inductance ratio define as $I_r = e_w^2 \sigma_w / (a^2 \sigma)$. With the hypothesis of moderate values of the magnetic Reynolds number R_m, the inductance ratio must be lower than 1, i.e.

$$I_r = \frac{e_w^2 \sigma_w}{a^2 \sigma} < 1.$$

This condition can be relaxed if the magnetic Reynolds number itself is much lower than 1.

It can be seen that if the wall is of finite depth, its conductivity cannot become infinite within the limits of the proposed theory.

Some of the formulations proposed in the present paper can be found in the Moreau book [9].

2. Formulation of the problem

2.1. Governing equations

The basic equations are

(i) The Maxwell equations,

$$\vec{\nabla} \wedge \vec{E} = -\frac{\partial \vec{B}}{\partial t} \quad \Rightarrow \quad \vec{\nabla} \cdot \vec{B} = 0, \tag{1}$$

$$\vec{\nabla} \wedge \vec{B} = \mu \vec{j} \quad \Rightarrow \quad \vec{\nabla} \cdot \vec{j} = 0, \tag{2}$$

(ii) the Ohm's law,

$$\vec{j} = \sigma(\vec{E} + \vec{V} \wedge \vec{B}), \tag{3}$$

(iii) the Navier–Stokes equation in which is included a term for the electromagnetic force,

$$\frac{\mathrm{d}\vec{V}}{\mathrm{d}t} = -\frac{1}{\rho}\vec{\nabla} p + \nu \cdot \Delta \vec{V} + \frac{1}{\rho}\vec{j} \wedge \vec{B} \quad \text{and} \tag{4}$$

(iv) the continuity equation, which is not explicitly used.

In these equations, $\vec{V}$ is the fluid velocity, $\vec{E}$ the electrical field, $\vec{J}$ the current density, p the pressure and $\nu = \mu/\rho$ the kinematic viscosity. The magnetic field $\vec{B}$, $\vec{B} = \vec{B_0} + \vec{b}$, is equal to the sum of the imposed and induced magnetic fields ($\vec{B_0}$ and $\vec{b}$ respectively).

The combination of Maxwell equations and Ohm's law gives the well-known induction equation,

$$\frac{\partial \vec{B}}{\partial t} = \vec{\nabla} \wedge \vec{V} \wedge \vec{B} - \frac{1}{\mu_0 \sigma} \Delta \vec{B}. \tag{5}$$

For the channel geometry it is assumed that $L_B \gg l \gg a$, which leads to the approximation:

$$\frac{\partial}{\partial x} \ll \frac{\partial}{\partial y}$$
$$\frac{\partial}{\partial z} \ll \frac{\partial}{\partial y}. \tag{6}$$

Considering the case of an established flow in x direction means that the velocity field can be written:

$$\vec{V} = u(y)\vec{e}_x. \tag{7}$$

Assuming that the induced magnetic field is much lower than the imposed one, the induced electric current $\vec{j}$ becomes:

$$\vec{j} = \begin{cases} j_x = \sigma E_x, \\ j_y = \sigma E_y, \\ j_z = \sigma(E_z + uB_y). \end{cases} \tag{8}$$

The equation of conservation of the electric current

$$\vec{\nabla} \cdot \vec{j} = \frac{\partial j_x}{\partial x} + \frac{\partial j_y}{\partial y} + \frac{\partial j_z}{\partial z} = 0$$

combined with the approximation (6) gives:

$$\frac{\partial E_x}{\partial x} \approx \frac{\partial E_z}{\partial z} \approx 0 \quad \Rightarrow \quad \frac{\partial E_y}{\partial y} = 0. \tag{9}$$

Assuming that there is no imposed voltage drop along the axial direction leads to $E_x = 0$. On the other hand, and because E_y vanishes inside the thin wall of the channel, the continuity of the y component of the current density at the interface between the wall and the fluid imposes that $E_y = 0$ everywhere. The value of E_z depends on the closure of the electrical current and thus on the value of load resistance R. To summarise the hypothesis, the electrical field distribution is assumed to be of the form:

$$\vec{E} = \begin{cases} E_x = 0, \\ E_y = 0, \\ E_z = E_z(y, R). \end{cases} \tag{10}$$

This distribution of the electrical field defines the form of the current density:

$$\vec{j} = \begin{cases} j_x = 0, \\ j_y = 0, \\ j_z = j_z(y). \end{cases} \tag{11}$$

Consequently the induced magnetic field has only a single component in x direction:

$$\vec{b} = \begin{cases} b_x, \\ 0, \\ 0. \end{cases} \tag{12}$$

2.2. Definition of the main variables

The imposed pressure distribution along the channel, which is the driving force of the flow, is assumed to be of the form:

$$p = p_0 + \mathrm{Re}\left(\frac{\Delta p}{L_B} x \mathrm{e}^{\mathrm{i}\omega t}\right) = p_0 + \mathrm{Re}\left(p_1 \mathrm{e}^{\mathrm{i}\omega t}\right) \tag{13}$$

where only the real part of the complex numbers are of physical interest. Other variables are supposed to have the same harmonically oscillating behaviours.

$$\begin{aligned} &u = \mathrm{Re}\left(u_0 \mathrm{e}^{\mathrm{i}\omega t}\right), \\ &\vec{B} = \vec{B}_0 + \vec{b} = \vec{B}_0 + b_x = \vec{B}_0 + b\mathrm{e}^{\mathrm{i}\omega t}. \end{aligned} \tag{14}$$

At the end of each cycle, the fluid comes back to its initial position and consequently the velocity has no mean value. The induced magnetic field b_x is the perturbation of the imposed magnetic field generated by the pulsating velocity.

2.3. Dimensionless analysis and governing dimensionless equations

By choosing the following characteristic typical scales: a for the length, B_0 for the magnetic field, $1/\omega$ for the time and ωa for the velocity, the scale for the electric current density can be defined as $B_0/(\mu_0 a)$ and for the typical electric field as $\omega a B_0$. Consequently the current scale $B_0 a/\mu_0$ and the electrical resistance per unit length of the channel $1/(\sigma a)$ allows us to define a typical scale for the electrical power $B_0^2 a/(\mu_0^2 \sigma)$.

Introducing the velocity and magnetic field distribution in the Navier–Stokes (4) and induction equations (5), neglecting the second order perturbation field (linearised equations), and taking into account the typical scales given above leads to the following dimensionless governing equations:

$$\mathrm{i}u^* = -K_p + \frac{1}{R_\omega}\frac{\partial^2 u^*}{\partial y^{*2}} + \frac{N}{R_m}\frac{\partial b_x^*}{\partial y^*}, \tag{15}$$

$$\mathrm{i}b_x^* = \frac{\partial u^*}{\partial y^*} + \frac{1}{R_m}\frac{\partial^2 b_x^*}{\partial y^{*2}} \tag{16}$$

with $K_p = \Delta p/(L_B \omega^2 \rho a)$ representing the dimensionless imposed driving pressure gradient, u^* and b^* are the dimensionless axial components of the velocity and induced magnetic field respectively. As can be seen in Eqs. (15) and (16), the physical phenomena are controlled by three parameters:

(1) The classical Reynolds number

$$R_\omega = \frac{\rho \omega a^2}{\mu}, \tag{17}$$

representing the ratio of inertia forces to viscous forces.

(2) The magnetic Reynolds number

$$R_m = \mu_0 \sigma \omega a^2, \tag{18}$$

which is the ratio of characteristic time of magnetic field diffusion to characteristic time of magnetic field convection, and

(3) the so-called interaction parameter

$$N = \frac{H_a^2}{R_\omega} = \frac{B_0^2 \sigma}{\omega \rho}, \tag{19}$$

which is the ratio of electromagnetic forces to inertia forces.

One can now introduce the Hartmann number,

$$H_a = \sqrt{N R_\omega} = B_0 a \sqrt{\sigma/\mu} \tag{20}$$

as the ratio of electromagnetic forces to viscous forces. This is often used in MHD flow studies. Thus the problem can be characterised by only three of the four independent dimensionless parameters defined above.

3. Analytical solution of the problem

3.1. General solution

Combining Eqs. (15) and (16) and assuming that $R_m \ll R_\omega$ gives a new system:

$$\frac{\partial^4 b_x^*}{\partial y^{*4}} - R_\omega (N + \mathrm{i}) \frac{\partial^2 b_x^*}{\partial y^{*2}} - R_\omega R_m b_x^* = 0, \tag{21}$$

$$\mathrm{i} u^* = -K_p + \frac{1}{R_\omega} \frac{\partial^2 u^*}{\partial y^{*2}} + \frac{N}{R_m} \frac{\partial b_x^*}{\partial y^*}. \tag{22}$$

The solution of Eq. (21) can be easily calculated and gives the following form for the induced magnetic field distribution:

$$b_x^* = C_1 \sinh(\alpha_1 y^*) + C_2 \sinh(\alpha_2 y^*) + C_3 \cosh(\alpha_1 y^*) + C_4 \cosh(\alpha_1 y^*). \tag{23}$$

Introducing this distribution of the induced magnetic field in Eq. (22) leads to an expression for the velocity profile:

$$\begin{aligned} u^* = {} & C_1 \left[\frac{\mathrm{i}}{\alpha_1} - \frac{\alpha_1}{R_m} \right] \cosh(\alpha_1 y^*) + C_2 \left[\frac{\mathrm{i}}{\alpha_2} - \frac{\alpha_2}{R_m} \right] \cosh(\alpha_2 y^*) \\ & + C_3 \left[\frac{\mathrm{i}}{\alpha_1} - \frac{\alpha_1}{R_m} \right] \sinh(\alpha_1 y^*) + C_4 \left[\frac{\mathrm{i}}{\alpha_2} - \frac{\alpha_2}{R_m} \right] \cosh(\alpha_2 y^*) + \mathrm{i} K_p \end{aligned} \tag{24}$$

with,

$$\alpha_1 = \sqrt{\frac{B + \sqrt{B^2 + 4C}}{2}}, \quad \alpha_2 = \sqrt{\frac{B - \sqrt{B^2 + 4C}}{2}}, \quad B = R_\omega (N + \mathrm{i}), \quad C = R_\omega R_m.$$

The system (23) and (24) needs four adequate boundary conditions to specify the values of C_1, C_2, C_3 and C_4.

3.2. Boundary conditions

The non-slip condition and symmetry of velocity and induced magnetic field gives:

$$u^*(y^* = 1) = 0, \tag{25}$$

$$\frac{\partial u^*}{\partial y^*}(y^* = 0) = 0, \tag{26}$$

$$b_x^*(y^* = 0) = 0. \tag{27}$$

A fourth condition is needed to specify the global solution. This will result from the closure of current density lines in the wall, in the fluid and in the load resistance. The closure of current lines is controlled by the electrical field. In the core of the channel the term $\vec{u} \wedge \vec{B}$ dominates the electrical field so the current lines pass through the channel, whereas in the vicinity of the walls the non-slip condition decreases the velocity and the electrical field becomes higher

than the $\vec{u} \wedge \vec{B}$ term, imposing an inverse electrical line distribution. To first order, the system can be represented by an equivalent electrical circuit (see Fig. 3), where the channel is replaced by a generator which have an equivalent internal resistance r traversed by a current I, and where the load R and the walls of the channel are two resistances in parallel, traversed respectively by currents I' and i. As in previous works (see for example [6,9]), the electrical boundary condition uses the concept of the load factor K which can be roughly interpreted as the ratio of the voltage at the load resistance (RI') over that produced by the generator $U = RI' - rI$ (I' and I have opposite sign). Using current conservation in the circuit, $I + i + I' = 0$, and taking into account the fact that the voltage drop inside the walls is equal to the voltage drop inside the load, i.e. $RI' = r_w I$, the load factor can be written in the form:

$$K = \frac{RI'}{RI' - rI} = \frac{RI'}{RI' - r(-i - I')} = \frac{RI'}{RI' + rI' + (rR/r_w)I'},$$

$$K = \frac{1}{1 + r/R + r/r_w}, \tag{28}$$

$$R = \frac{r}{(1-K)/K - \sigma_w e_w/(\sigma a)}. \tag{29}$$

In the definition (28) of the load factor, $r = l/(\sigma a L_B)$ is the internal resistance of the fluid and $r_w = l/(\sigma_w e_w L_B)$ the wall resistance. So it is of use in the following to introduce the conductance ratio $C_w = \sigma_w e_w/\sigma a$ which characterises the ratio of wall conductance over fluid conductance.

If the load resistance R vanishes, $K = 0$. This corresponds to a short circuit configuration, and the power output vanishes. If $R \to \infty$ the current lines close in the walls and in the fluid and the power output is again zero. Moreover if the walls are insulating, $K = 1$, the current lines can only close within the fluid. In the case of a perfect system characterised by a closure of the electrical lines only in the external finite resistance, K is (to the first order) the power consumed in the load resistance over the power produced by the MHD channel. This parameter is consequently connected to the electrical efficiency of the system.

In the definition for the final boundary condition, the electrical current in the fluid can be expressed as a function of b_x,

$$I = \iint (\vec{j} \cdot \vec{e}_z)\,\mathrm{d}x\,\mathrm{d}y = -\frac{L_B B_0}{\mu_0} \int_{-1}^{1} \frac{\mathrm{d}b_x^*}{\mathrm{d}y^*}\mathrm{d}y^*,$$

$$I = -\frac{2L_B B_0}{\mu_0} b_x^*(y^* = 1). \tag{30}$$

Using the thin wall approximation and assuming continuity of the electrical field at the liquid/wall interface ($y^* = 1$) gives:

$$E_z(y = a) = \frac{j_w}{\sigma_w} = \frac{j(y = a)}{\sigma}, \tag{31}$$

the subscript w referring to the "wall". The current density at the wall can also be expressed as a function of b_x:

$$\begin{aligned} i &= \iint (\vec{j} \cdot \vec{e}_z)\,\mathrm{d}x\,\mathrm{d}y = -2L_B e_w j_w = 2L_B e_w \frac{\sigma_w}{\sigma} j(y = a), \\ i &= -2L_B \frac{\sigma_w e_w}{\sigma a} \frac{B_0}{\mu_0} \frac{\mathrm{d}b_x^*}{\mathrm{d}y^*}(y^* = 1). \end{aligned} \tag{32}$$

Considering that, according to Fig. 3, the external load and the wall resistances are in parallel and then submitted to the same voltage drop, the electrical current in the load takes the form:

$$I' = \frac{(E_z)_{y=a} 2l}{R} = -\frac{2B_0}{a\sigma R \mu_0} \left(\frac{\mathrm{d}b_x^*}{\mathrm{d}y^*}\right)_{(y^*=1)}. \tag{33}$$

Taking into account the continuity of the electrical current at the electrode, $I + I' + i = 0$, leads to the following expression for the fourth boundary condition:

$$b_x^*(y^* = 1) = \frac{K-1}{K}\frac{\partial b_x^*}{\partial y^*}(y^* = 1) \quad \text{or}$$
$$b_x^*(y^* = 1) = \beta\frac{\partial b_x^*}{\partial y^*}(y^* = 1), \quad \beta = \frac{K-1}{K}. \tag{34}$$

3.3. Analytic and asymptotic solutions

These four boundary conditions allow the determination of the four constants of integration in Eqs. (23) and (24):

$$C_1 = \frac{-\mathrm{i}K_p}{A^*\cosh(\alpha_1)}\frac{1}{1-((\tanh\alpha_1-\beta\tanh\alpha_1)/(\tanh\alpha_2-\beta\tanh\alpha_2))B^*/A^*}, \tag{35}$$
$$C_2 = -\mathrm{i}K_p\frac{\beta\alpha_1-\tanh\alpha_1}{[\tanh\alpha_2-\beta\alpha_2-(B^*/A^*)(\tanh\alpha_1-\beta\alpha_1)]A^*\cosh\alpha_2}, \tag{36}$$
$$A^* = \frac{\mathrm{i}}{\alpha_1}-\frac{\alpha_1}{R_m}, \qquad B^* = \frac{\mathrm{i}}{\alpha_2}-\frac{\alpha_2}{R_m},$$
$$C_3 = 0, \tag{37}$$
$$C_4 = 0, \tag{38}$$

and consequently fix the solution of the problem.

This solution takes a simplified form in the two asymptotic cases corresponding to high values of the interaction parameter N:

$$C_1 \cong \frac{-K_pR_m}{H_a\cosh H_a}\left(\frac{1}{\mathrm{i}+(1-K)N}\right), \qquad C_2 \cong \mathrm{i}K_p\sqrt{\frac{R_m}{N}}\left[\frac{N(K-1)}{1+\mathrm{i}N(K-1)}\right]. \tag{39}$$

In the derivation of the expressions (39) the following approximations have been used,

$$A^* \cong -\frac{H_a}{R_m}, \qquad B^* \cong \sqrt{\frac{N}{R_m}},$$

which leads to simplified expressions for both the velocity and induced magnetic field:

$$u^* \cong \frac{K_p}{\mathrm{i}+(1-K)N}\left[\mathrm{e}^{H_a(y^\bullet-1)}-1\right], \quad b_x^* \cong \frac{K_pR_m(1-K)}{\mathrm{i}+(1-K)N}y^*. \tag{40}$$

In contrast, for small values of the interaction parameter the expressions (35) and (36) of the two constants C_1 and C_2 become:

$$C_1 \cong \frac{\mathrm{i}K_pR_m}{\sqrt{\mathrm{i}R_\omega}\cosh\sqrt{\mathrm{i}R_\omega}}, \qquad C_2 \cong (K-1)K_p\sqrt{\mathrm{i}R_m}, \tag{41}$$

in which the following approximations have been used:

$$A^* = \frac{-\sqrt{\mathrm{i}R_\omega}}{R_m}, \qquad B^* \approx 0.$$

This results in the expressions:

$$u^* \cong \mathrm{i}K_p\left(1-\mathrm{e}^{\sqrt{\mathrm{i}R_\omega}(y^*-1)}\right), \qquad b_x^* \cong \mathrm{i}(K-1)K_pR_my^*. \tag{42}$$

4. Results and discussion

4.1. Velocity and magnetic field evolution

The solutions of Eqs. (23) and (24) with the proper values of the constant C_1, C_2, C_3 and C_4 given by the expressions (35)–(38) versus the parameters R_m, R_ω, N and K are presented on Figs. 4–6. The main values used for the dimensionless parameters are given on Table 1. These values correspond to the use of the liquid sodium.

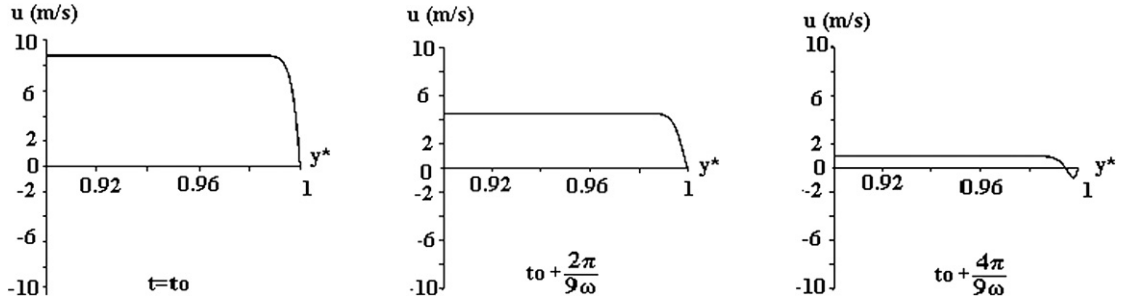

Fig. 4. Velocity profile near the wall ($0.9 < y^* < 1$) for three successive instants separated by a period of time equal to $2\pi/9\omega$, for conditions corresponding to Table 1 and for $N = 1$. The phase shift, due to the viscosity, between the core of the flow and the boundary layers can be seen clearly.

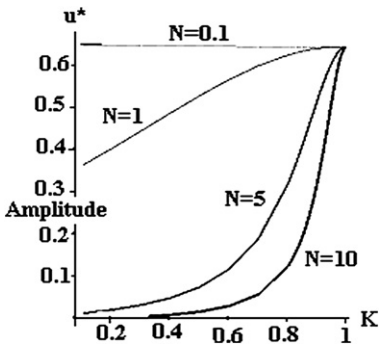

Fig. 5. Dimensionless velocity amplitude $u^*(y^* = 0)$ versus load factor K for $R_m = 0.33$, $R_\omega = 132974$ and four values of N.

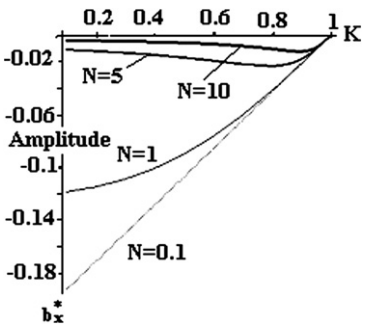

Fig. 6. Dimensionless induced magnetic field amplitude $b^*(y^* = 0.99)$ versus load factor K for $R_m = 0.33$, $R_\omega = 132974$, and four values of N.

Table 1
Principal values used for the numerical applications

R_m	R_ω	K_p	C_w	R
0.3333	132974	0.6426	0.07286	$0.0000182/((1/K) - 1.072986)$

Fig. 4 shows the velocity profile at different instants in a velocity cycle for $N = 1$. A phase shift can be clearly observed between the core velocity and the velocity distribution inside the boundary layers. This phase shift is generated by the viscosity that reduces the amplitude of the inertia forces near the walls.

Figs. 5 and 6 show the evolution of both velocity and induced magnetic field versus the load factor K for fixed values of magnetic Reynolds number R_m and Reynolds number R_ω and four values of the interaction parameters N. It can be seen that the velocity decreases when the interaction parameter increases. This results from the influence of the electromagnetic forces (opposed to the driving pressure gradient) which increases when the magnetic field and the Hartmann number increase. The results represented by the two figures can be easily interpreted by using the asymptotic solutions given by expressions (40) and (42).

It can be seen also in Fig. 5 that for a load factor close to 1, all the curves converge towards a single value. This can be explained by the fact that, to first order, the electrical current is confined to the cross-section of the channel and the integral of the current density, the total electric current, is equal to 0. Consequently the global electromagnetic force vanishes. With this condition the intensity of the velocity depends on the equilibrium between the driving pressure gradient and the inertia forces. Zooming on the point of convergence in Fig. 5 it can be observed that both the velocity and induced magnetic field values show a small dependence on the interaction parameter that will be explained later (see for example Fig. 11).

Fig. 6 represents the evolution of the induced magnetic field in the vicinity of the wall (for $y^* = 1$) versus the load factor. This goes to 0 when K tends to 1. This is in agreement with Eq. (34) which characterises the closure of the

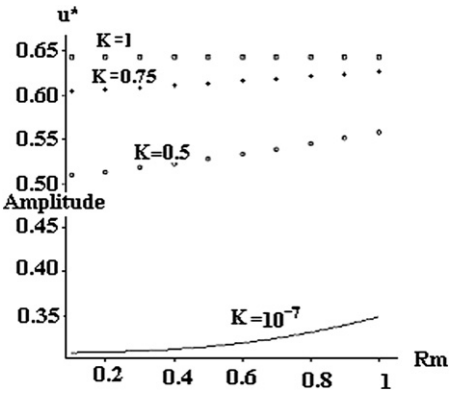

Fig. 7. Dimensionless velocity amplitude $u^*(y^* = 0)$ versus R_m for $N = 1$, $R_\omega = 132974$, and four values of K.

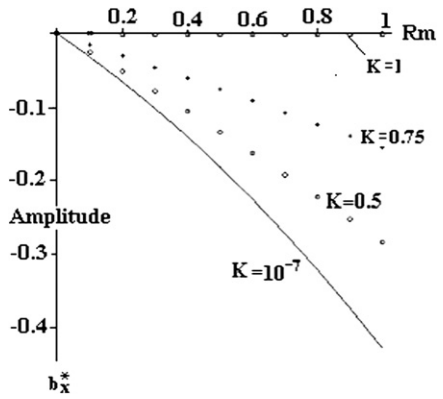

Fig. 8. Dimensionless induced magnetic field amplitude $b^*(y^* = 0.99)$ versus R_m for $N = 1$, $R_\omega = 132974$ and four values of K.

electric current; when $K = 1$, b_x is equal to 0. On the other hand it can be observed that all the curves have a common slope for $K = 1$. This can be interpreted in the following manner: In the vicinity of the wall and for values of K close to 1 the current density is:

$$J_{z\cong a} \cong \sigma E_z \cong -\sigma u_0 B_0 \cong -\frac{\partial b_x}{\partial y}(y \cong a). \tag{43}$$

Using the induced magnetic field gradient expression given by (34) leads to:

$$b_x(y = a) = \mu_0 \sigma u_0 a B_0 \frac{K-1}{K} = R_m B_0 u_0^* \frac{K-1}{K}. \tag{44}$$

For $K \cong 1$, the amplitude of velocity, $u_0^* \approx K_p$ results essentially on the equilibrium between inertia and pressure forces. In dimensionless form, this becomes:

$$\left(\frac{\partial b_x^*}{\partial K}\right)_{K\cong 1} \cong \left(\frac{K_p R_m}{K^2}\right)_{K\cong 1}. \tag{45}$$

Thus the slope of all the curves, $\partial b_x^*/\partial K$, converges toward the value of the product $(K_p R_m)$ when K approaches 1. This is also in agreement with the simplified formula corresponding to $N \gg 1$ (40) or to $N \ll 1$ (42).

Figs. 7 and 8 show the maximal amplitudes of velocity and induced magnetic field versus the magnetic Reynolds number R_m for fixed interaction parameter N and Reynolds number R_ω and four load factors K.

It can be seen in Fig. 7 that for a given value of the magnetic Reynolds number the velocity increases when the load factor increases, in agreement with Fig. 5. It can be seen also that for large R_m all the curves seem to converge to the asymptotic value obtained for $K = 1$ (even if, on the figure, the values of R_m are limited to 1). This can be explained easily; when R_m increases, the depth of penetration, δ, of the induced magnetic field b_x which is in the liquid media of order,

$$\frac{\delta}{a} \approx \sqrt{\frac{1}{R_m}},$$

decreases. When R_m tends to infinity the magnetic field is confined to the edge of the flow and the electromagnetic forces vanish almost everywhere else. In that case the flow is controlled again by an equilibrium between the inertia forces and the driving pressure gradient.

Fig. 8 shows the evolution of the induced magnetic field versus the magnetic Reynolds number. Clearly the induced field increases (for small or moderate R_m values) when R_m is increasing and decreases when the load factor K increases. This results from the fact that when K increases, the current density in the generator decreases as does the induced field.

Figs. 9 and 10 show the maximum amplitudes of velocity and induced magnetic field versus the interaction parameter N for fixed Reynolds and magnetic Reynolds number, R_ω and R_m respectively, and different values of the load factor K.

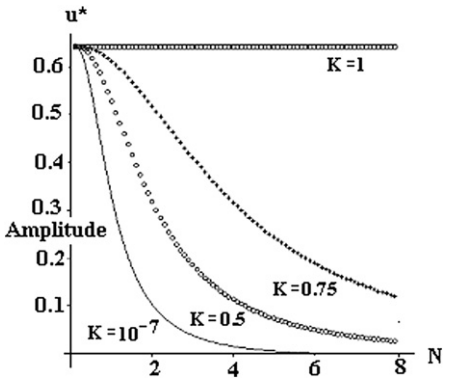

Fig. 9. Dimensionless velocity amplitude $u^*(y^* = 0)$ versus N, $R_\omega = 132974$, for $R_m = 0.33$ and four values of K.

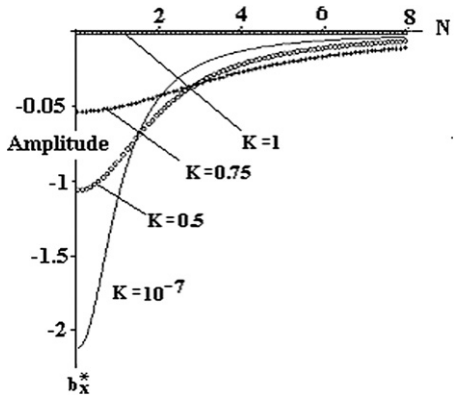

Fig. 10. Dimensionless induced magnetic field amplitude $b^*(y^* = 0.99)$ versus N for $R_\omega = 132974$, $R_m = 0.33$, and four values of K.

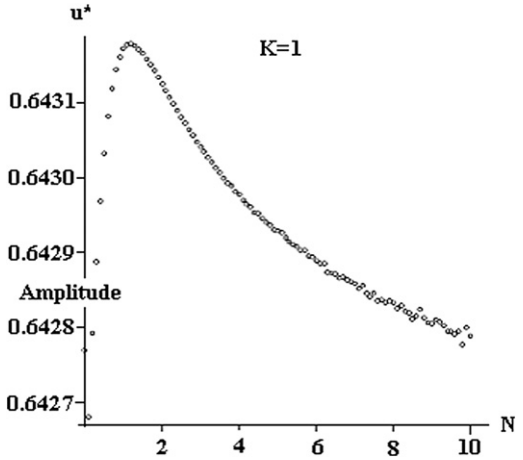

Fig. 11. Zoom of the characteristic point of Fig. 6: Evolution of u^* versus N for $K = 1$.

It is clear from Fig. 9 that for low values of the interaction parameter, the effect of the electromagnetic forces can be neglected and the velocity is again controlled by an equilibrium between the inertia and pressure force. On the contrary when the interaction parameter takes large values, the electromagnetic forces opposed to the pressure forces are responsible for the decrease in the velocity that tends asymptotically to zero for infinite value of N. This effect is more pronounced for small load factors corresponding to a high current density distribution.

The interpretation of Fig. 10 is of the same nature. When the interaction parameter increases, the flow velocity decreases and the dimensionless induced current decreases (but the electromagnetic forces proportional to B_0^2 increase nevertheless). This corresponds to a decrease in the dimensionless induced field that leads to zero for high values of the interaction parameter. This effect is more pronounced for lower values of the load factor corresponding to higher current density.

Considering the particular case of load factor equal to 1 and operating a zoom on the evolution of the velocity versus the interaction parameter, it can be seen that even if u^* seems to be constant in Fig. 9, Fig. 11 reveals a characteristic evolution which can be interpreted by considering two regimes of flow: The Hartmann and Inertia regimes. For low values of N (Inertia regime), the electrical lines generated in the core of the flow close in the viscous layer controlled by the oscillation frequency ω. In this case, when N increases (or ω decreases) the depth of the boundary layer increases. Thus the global electrical resistance of the boundary layer decreases. Consequently that part of the electrical current closing in the layer and the boundary layer electromagnetic force increases. This force directed in the same sense as the driving pressure gradient increases the velocity (Fig. 11). This evolution ceases when the depth of the

Hartmann layer becomes of the same order as the depth of the inertia layer, i.e. for an interaction parameter equal to 1. For higher values ($N > 1$) (the Hartmann regime) when N increases, the flow becomes controlled by the Hartmann layer that decreases when N or H_a increases. The electromagnetic forces in the core flow increase and the velocity decreases. The transition between the two regimes takes place for an interaction parameter near to 1. In all the cases (for any value of N) the net current, sum of the electric current in the core and in the layers, is near to zero for this particular case of load factor equal to 1. The magnetic field follows roughly the same evolution (not represented). For small N when the velocity increases the intensity of both the induced electrical current and magnetic field increases. After this first phase, the dimensionless induced field decreases, mainly because the velocity decreases for N larger than 1.

4.2. Closure of the AC current with respect of boundary layers and walls characteristics

The physical explanation of the hydrodynamics and electrical regime that control the process can be summarised as follows. The imposed alternating driving pressure forces are mainly balanced by both the electromagnetic forces (Lorentz/Laplace forces) controlled by the magnetic field, and the inertia forces associated with the oscillation. Consequently, two boundary layers are in competition in the system: The oscillating (viscous/inertia) layer of thickness,

$$\delta_\nu \approx \sqrt{\frac{\mu}{\omega\rho}},$$

similar to the Ekman layer in a rotating fluid [10], and the Hartmann layer of thickness a/H_a [6]. Depending on the pulsation ω and on the magnetic field intensity, one of these two layers controls the closure of the induced electric current. For high oscillation frequencies for example (small values of N), the thickness of the boundary layer is controlled by inertia. In this case the electric current closes in the oscillating (or inertia/viscous) layers. This situation is referred to as the "inertia regime". In contrast, for a large asymptotic magnetic field the electromagnetic forces dominate and the induced electrical current closes classically in the Hartmann layer. This is referred to as the Hartmann regime.

Each boundary layer can be characterised by a conductance ratio, C_{H_a} for the Hartmann layer, and C_ω for the oscillating viscous layer:

$$C_{H_a} = \frac{\sigma\delta_{H_a}}{\sigma a} = \frac{1}{H_a}, \tag{46}$$

$$C_\omega = \frac{\sigma\delta_\nu}{\sigma a} = \sqrt{\frac{2\mu}{\omega\rho a^2}}. \tag{47}$$

The comparison between the wall conductance ratio C_w, and the conductance ratio characterising the two boundary layers C_{H_a} and C_ω gives the preference for the induced current to close in the wall or in one of the two layers. If $C_w/C_{H_a} \gg 1$ and $C_w/C_\omega \gg 1$ the wall can be considered as perfectly conducting and the current lines close preferentially in the wall; conversely if $C_w/C_{H_a} \ll 1$ or $C_w/C_\omega \ll 1$, the wall can be considered as isolating and current lines close preferentially in one of the two layers. This case $C_{H_a} > C_\omega$ corresponds to the Hartmann regime, while $C_{H_a} < C_\omega$ corresponds to the inertia regime. Fig. 12 schematically summarises the different situations.

4.3. Efficiency

The efficiency corresponds to the ratio between the electrical power extracted from the load and the mechanical energy introduced in the system by the work of the driving pressure forces. Since the electrical circuit is assimilated to a load resistance R, the electrical power P_e created to supply this circuit is simply the power dissipated by the Joule effect in this resistance,

$$P_e = \overline{RI'^2}, \tag{48}$$

the bar denoting the average on a period. The total efficiency of the system is then defined by:

$$\eta_e = \frac{P_e}{P_e + P_1 + \cdots + P_n}, \tag{49}$$

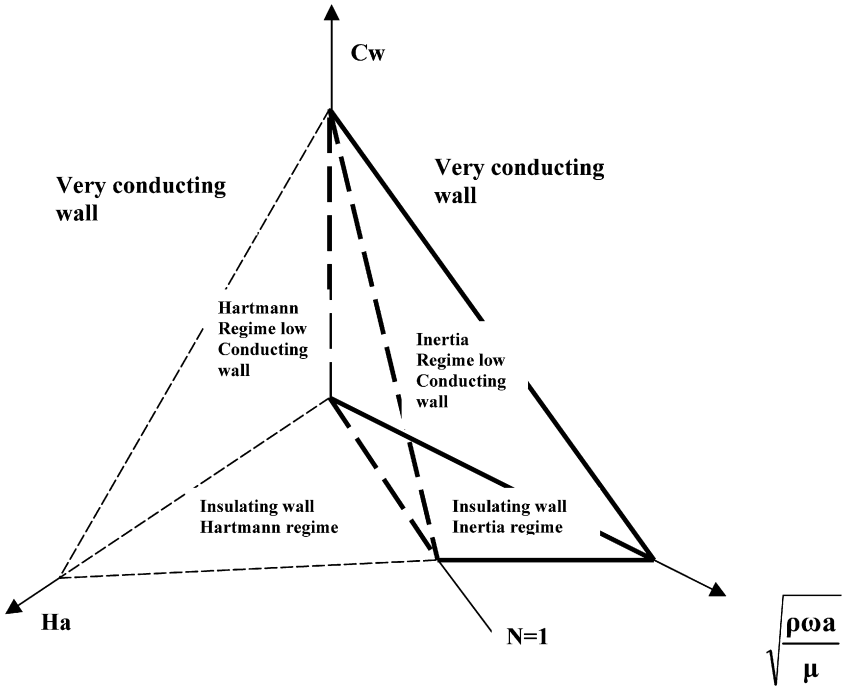

Fig. 12. Graph representing the different regimes of flows i.e. Hartman regime, inertia regime, conducting or insulating wall regimes. The dashed line represents the region with small conductance ratio and small pulsation: the Hartmann regime. The bold line represents the region with small conductance ratio and small Hartmann number: the inertia regime. The volume over represents the region with high conducting walls.

$P_1, \ldots, P_n$ being the power losses. There are two types of power losse, the Joule effect P_J in the fluid and in the walls and the hydrodynamic viscous losses P_μ. They are defined by the following relations,

$$P_j = 2lL_B \int_{-a}^{a} \frac{\overline{J^2}}{\sigma}\,\mathrm{d}y + \overline{r_w i^2} = \frac{lL_B B_0^2}{\mu_0 \sigma a} \int_{-1}^{1} \left|\frac{\mathrm{d}b_x^*}{\mathrm{d}y^*}\right|^2 \mathrm{d}y^* + \overline{r_w i^2}, \tag{50}$$

$$P_\mu = 2lL_B \int_{-a}^{a} \mu u \frac{\overline{\mathrm{d}^2 u}}{\mathrm{d}y^2}\,\mathrm{d}y = lL_B \mu\omega \int_{-1}^{1} \mathrm{Re}\left[\tilde{u}_x^* \frac{\mathrm{d}^2 u_x^*}{\mathrm{d}y^{*2}}\right] \mathrm{d}y^*, \tag{51}$$

r_w and i being the resistance and the electrical current in the walls of the channel respectively. The tilde denotes complex conjugation and the bar the mean value over one period of oscillation, while Re designates the real value of the quantity in the bracket.

Neglecting the viscous losses, the electrical efficiency is defined as:

$$\eta_e = \frac{P_e}{P_e + P_J}. \tag{52}$$

It can be observed in Fig. 13, that the evolution of the efficiency versus the Reynolds number R_ω for small R_m, $K = 0.5$, $H_a = 500$ and insulating walls, is in perfect agreement with the results of Ibanez et al. [8].

The observation (Fig. 13) confirms the existence of two asymptotic regimes. The zone such as $R_\omega < 10^5$ corresponds to the Hartmann regime. In this case a part of the electrical current closes inside the Hartmann layer that decreases when H_a increases, producing an improvement of the efficiency. For a given Hartmann number the electrical efficiency conserves a constant value for low values of the Reynolds number. This regime is maintained until the Hartmann layer reaches the same value as the viscous layer controlled by inertia, corresponding to a value of the interaction parameter equal to 1. For $R_\omega > 10^5$ the inertia/viscous layer (of thickness $\sqrt{\mu/\omega\rho}$), becomes lower than the Hartmann layer corresponding to the inertia regime and a part of the electrical current closes inside this layer

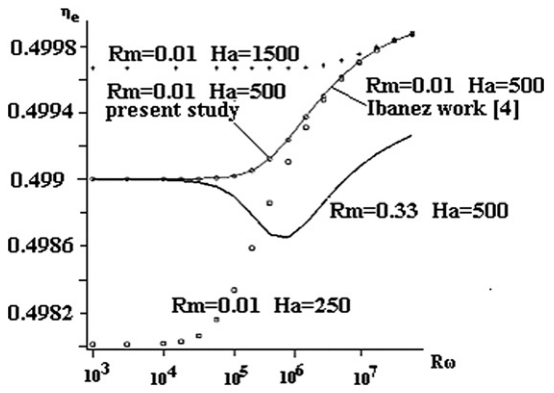

Fig. 13. Electrical efficiency versus Reynolds number for $R_m = 0.01$ and $R_m = 0.33$ and for $R_\omega = 13297$, insulating walls, $K = 0.5$, and three values for H_a. The curves for small R_m are in agreement with Ibanez et al. [8]. The curve for $R_m = 0.33$ presents a decrease in efficiency around $N = 1$ at the transition between the Hartmann and inertial regimes.

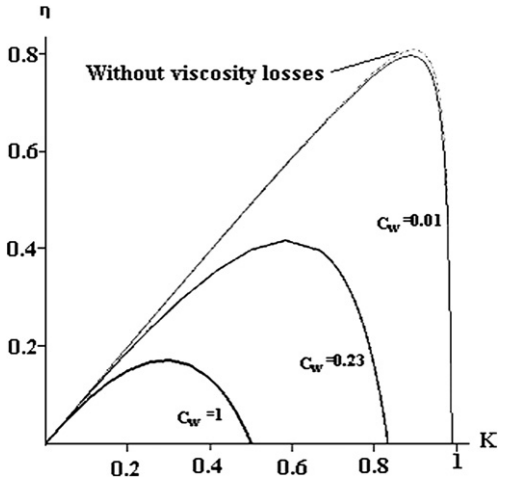

Fig. 14. Efficiency of the generator versus the load factor K for three conductance ratios, $C_w = 0.01$, $C_w = 0.2$ and $C_w = 1$. The other parameters are indicated in Table 1. It can be seen that the efficiency decreases when the conductance ratio increases. For $C_w = 0.01$ the efficiency is characterised by two curves, one without the viscous losses and the other one with the viscous losses. As can be seen the influence of the viscosity is not very important in this range of parameters.

which decreases when the pulsation increases. So that part of the electrical current closing in this layer decreases gradually with increasing ω, corresponding to an improvement in the efficiency. For large R_ω the efficiency tends to a maximum value that can be observed in Fig. 13. On the other hand it can be observed also that when the magnetic Reynolds number is not negligible, say for example for $R_m = 0.33$, the evolution of the efficiency versus R_ω presents noticeable differences with the results obtained by Ibanez et al. [8] for very small magnetic Reynolds numbers. In this case and for $R_\omega < 10^5$ (Hartmann regime) the decrease in electrical efficiency versus R_ω results from the pulsation of the induced magnetic field producing a superimposed electrical current distribution which does not contribute to supply the load but generates additive Joule losses which increase when ω and consequently R_ω increase. The same phenomenon explains why the asymptotic value in the inertia regime is lower than that obtained for small R_m.

The total efficiency of the system taking account all losses is defined as:

$$\eta = \frac{P_e}{P_e + P_J + P_\mu}, \tag{53}$$

and can be plotted as a function of the parameters K, R_m and N (see Figs. 14, 15).

Fig. 14 represents the typical evolution of the efficiency versus the load factor for different values of the conductance ratio. It can be seen that the efficiency vanishes for two typical values of the load factor corresponding to $K = 0$ (the load resistance is zero), and $K = 1/(1 + C_w)$ (the load resistance becomes infinite). The maximum efficiency attainable is located between these two values and depends of the conductance ratio, insulating walls being optimal. It is clear that a part of the electric current passes inside the walls when they are conducting ($C_w > 0$),thus reducing the efficiency. On the other hand for $C_w = 0.01$ the evolution of efficiency was calculated with and without viscous losses. The small difference that can be observed at the maximum of the curves characterises this effect. It is negligible in the range of parameters used in the present study. Fig. 15 summarises the interpretation of Fig. 14 and shows that when the conductance ratio increases, the maximum efficiency attainable decreases due to the by-pass of an increasing part of the electrical current created in the core, inside the wall of the generator. It must be mentioned that the maximum efficiency does not correspond exactly to the maximum power that can be extracted from the process. For space applications for example, the concept of power density (i.e. the power per unit mass) is the most important factor.

The evolution of the maximum efficiency versus the magnetic Reynolds number (not represented) is such that, for very small magnetic Reynolds numbers, the efficiency increases against R_m and reaches a maximum value (cor-

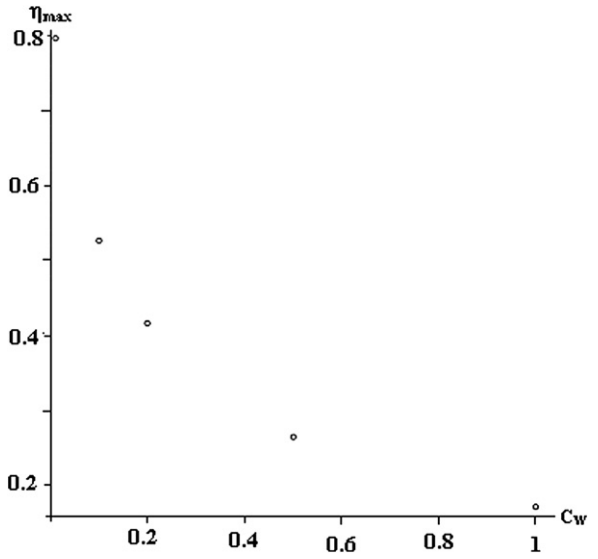

Fig. 15. Maximum efficiency attainable versus wall conductance ratio C_w.

responding roughly to $N = 1$). Thereafter the efficiency decreases slowly due to improvement of the Joule effect generated by the pulsation of the induced magnetic field.

5. Conclusion

This study focused on the characterisation of an alternate MHD generator resulting from the use of the thermo-acoustic effect to impose an oscillating driving pressure gradient. The effect of wall conductivity has been taken into account and a solution found for small or moderate values of the magnetic Reynolds number. The role of the main parameters that control the efficiency, i.e. the interaction parameter, the Reynolds number, the magnetic Reynolds number, the load factor and the conductance ratio, has been analysed. Full optimisation of the system is not within the scope of the present paper and requires a special study. Nevertheless, some indications can be given; the best efficiency is obtained for relatively high values of the load factor ($K > 0.8$), moderate values of the interaction parameters ($N > 1.5$), and for values of the magnetic Reynolds number close to 1. It is important to note here that the influence of this last parameter is generally neglected in most studies.

It must be noted that, the electric current produced by this system using the conducting process is delivered at low voltage and high intensity which is not necessarily best adapted for general use. It is the possibility offered by the pulsating induced magnetic field (to increase the voltage level and decrease the intensity of the electric current) that makes further work on induction process essential

References

[1] G.W. Swift, Thermoacoustic engines, J. Acoust. Soc. Am. 84 (4) (1988) 1145–1180.
[2] R.J. Rosa, Magnetohydrodynamic Energy Conversion, Hemisphere Publishing Corporation, New York, 1987.
[3] R. Laborde, A. Alemany, F. Werkoff, Performance capabilities of a space-power liquid metal MHD converter, Acta Astronaut. 19 (4) (1989).
[4] H. Branover, Y. Unger, Metallurgical Technologies, Energy Conversion, and Magnetohydrodynamic Flows, Progress in Astronautics and Aeronautics, vol. 148, 1992.
[5] S. Molokov, Fully developed liquid metal flow in multiple rectangular ducts in a strong magnetic field, Eur. J. Mech.(6) (1993) 769–787.
[6] A. Kharicha, A. Alemany, D. Bornas, Influence of the magnetic field and the conductance ratio on the mass transfer rotating lid driven flow, Int. J. Heat Mass Transfer 47 (2004) 1997–2014.
[7] S. Cuevas, B.F. Picologlou, Liquid-metal flow in rectangular ducts with thin conducting or insulating walls: laminar and turbulent solutions, Int. J. Engrg. Sci. 35 (5) (1997) 485–503.
[8] G. Ibanez, S. Cuevas, M. Lopez de Haro, Optimization analysis of an alternate MHD generator, Energy Conversion and Management 43 (2002) 1757–1771.
[9] R. Moreau, Magnetohydrodynamic, Kluwer, Dordrecht, 1990.
[10] H. Schlichting, Boundary Layer Theory, McGraw-Hill, New York, 1988.